Journal of Power Sources 672 (2026) 239657

Contents lists available at ScienceDirect

Journal of Power Sources

journal homepage: www.elsevier.com/locate/jpowsour

Lithium electrode growth regime due to solid electrolyte interphase: A multiphase-field approach

Thibault Delpech [a], Benoit Chavillon [a], Sébastien Martinet [a], Anass Benayad [b], Hervé Manzanarez [a],*

[a] Univ. Grenoble Alpes, CEA, Liten, 38000 Grenoble, France
[b] Institute for Applied Materials (IAM), Karlsruhe Institute of Technology (KIT), 76344 Eggenstein-Leopoldshafen, Germany

HIGHLIGHTS

- A multiphase field model describes chemical complexity at lithium metal interfaces.
- The model reveals mechanisms driving lithium dendrite nucleation.
- Two distinct dendrite nucleation modes are identified and characterized.
- Key parameters controlling dendrite nucleation are quantified.

ARTICLE INFO

Keywords:
Lithium metal
Solid electrolyte interphase
Multiphase-field modeling
Dendrite nucleation

ABSTRACT

The solid electrolyte interphase (SEI) plays a critical role in controlling the current distribution at the lithium electrode/electrolyte interface. The heterogeneous nature of lithium deposition leads to dendrite formation. To address this, we develop a multiphase-field model to investigate the role of a heterogeneous SEI in dendrite nucleation during electrodeposition. We first propose a qualitative study to characterize lithium growth regimes and define an observable mechanism to identify SEI failure modes leading to dendrite nucleation. Finally, a parametric study of the SEI structure highlights the key characteristics that can drive the nucleation of lithium dendrite.

1. Introduction

Lithium metal electrodes are promising candidates for all-solid-state batteries because of their high energy density and lower electrochemical potential, compared to conventional intercalation electrodes. However, heterogeneous lithium electrodeposition leads to the growth of dendritic lithium patterns [1–3], resulting in dendritic growth patterns. This phenomenon can potentially cause short circuits or reduce coulombic efficiency of the battery and owing to the loss of active material. From a theoretical point of view, at high current density, the dendrite formation can be predicted using the Sand's theory [4]. Nevertheless, the observation of dendrites even at low current density [5] suggests that the local current density is subject to large fluctuations at the electrode/electrolyte interface, leading to the creation of preferential deposition areas. This interface has been extensively investigated in several studies [6–12], showing the formation of a heterogeneous passivation layer, called Solid Electrolyte Interphase (SEI), to chemically stabilize the lithium electrode. The formation of SEI is observed in both liquid [2,3] and solid electrolytes [13,14]. The structure, composition and mechanical properties of the SEI depend on multiple parameters, including the composition of the electrolyte [15,16], temperature [17], operating conditions [18], and certainly the roughness of the lithium electrode. This strong dependence on multiple parameters has so far hindered the development of a universal SEI model capable of accurately capturing experimental observations at the local scale. Multilayer [19] and mosaic [20] models have been proposed as initial approaches to describe and better understand the structure of the SEI. Insight into the SEI remains a significant challenge, with many questions still unsolved, particularly regarding its role in dendrite nucleation. The heterogeneous nature of its properties gives rise to localized "hot spots" related to surface roughness, preferential lithium-ion conduction, pathways determined by chemical inhomogeneities, and regions of enhanced deformability associated with mechanical heterogeneity. The limited spatial resolution of *in situ* techniques makes it difficult to probe nanoscale heterogeneities in SEI properties. To

---

* Corresponding author.
E-mail address: herve.manzanarez@cea.fr (H. Manzanarez).

https://doi.org/10.1016/j.jpowsour.2026.239657
Received 19 December 2025; Received in revised form 28 January 2026; Accepted 14 February 2026

overcome this limitation, computational approaches have been employed to investigate the role of the SEI in lithium dendrite growth. *Ab initio* methods, in particular, have been widely used to study the SEI formation, ionic transport, and mechanical properties. However, their applicability remains constrained by the small system sizes they can handle, typically only a few nanometers. These methods highlight the heterogeneous nature of the SEI [9,21], but they lack the ability to track dendritic growth. At larger scale, continuum models have been developed to study dendrite geometries [22–26] to propose new cycling protocols to suppress their formation. However, the scale difference between the dendrite size and SEI thickness has led several models to neglect the SEI. Recent works have considered the SEI with homogeneous transport properties [11,24–26]. In addition, mechanical effects have been considered [11,25], particularly to investigate SEI failure mechanisms [11].

As far as we know, only a few studies [12,27] have been conducted using a stationary multidomain SEI. We aim to develop a new approach to better understand how lithium-ion deposition initially deforms the lithium-SEI interface. We employed a multiphase-field method to investigate the dynamic behavior of a heterogeneous multidomain SEI under polarization. This approach enables us to capture the evolution of the SEI, with particular emphasis on its ability to delay cracking, a key process leading to dendrite nucleation. Beyond this specific application, the proposed model is broadly applicable to non-equilibrium system involving chemical reactions.

2. System modeling

To investigate the interface between lithium metal and SEI, we consider a system comprising $N = 4$ domains: the electrode, the electrolyte and two distinct SEI domains with different properties. Each domain is associated with a phase i and an order parameter ξ_i. Each ξ_i represents a conserved continuous variable ranging from 0 to 1. Therefore, all ξ_i indicate the presence of the phase i ($\xi_i \rightarrow 1$) or the absence ($\xi_i \rightarrow 0$) at a given position. Between these limits, the system is in a diffuse interface regime.

For the following, variables with the index $i = 0$ are associated with an electrolyte, $i = 1$ with a lithium metal electrode, $i = 2$ and $i = 3$ with (different) SEI domains. The presented model is valid for systems with an arbitrary phase number N.

The total free energy of the system is assumed to be

$$\mathcal{F}_{tot} = \sum_{i=0}^{N-1} \mathcal{F}_i \left[\xi_i\right] \tag{1}$$

where $\mathcal{F}_i$ is the free energy of the phase i, defined by the Ginzburg–Landau free energy:

$$\mathcal{F}_i \left[\xi_i\right] = k_B T \int_{\Omega} \left[W_i f\left(\xi_i\right) + \frac{1}{2}\kappa_i \left\|\vec{\nabla}\xi_i\right\|^2 \right] dV \tag{2}$$

with f a free energy density, which is an arbitrary double-well function defined as $f\left(\xi_i\right) = \xi_i^2\left(1-\xi_i\right)^2$ and whose stable equilibria are the extrema values of ξ_i. W_i (in units of J.m^{-3}) and κ_i (in units of J.m^{-1}) are respectively the barrier height and the gradient energy coefficient associated with ξ_i. From these parameters, the dimensionless energy surface tension $\gamma_i = \sqrt{W_i \kappa_i}$ and the typical length $\lambda_i = \sqrt{\frac{\kappa_i}{W_i}}$ associated with phase i are defined. The typical length λ_i is proportional to the size of the diffuse interface. The surface tension γ_i represents the energetic cost associated with the formation of a diffuse interface. To ensure symmetrical interfaces, the same characteristic length is assigned to all phases (i.e. $\lambda = \lambda_i \quad \forall i$), which prevents artificial asymmetries in the interfacial properties and ensures numerical consistency in the model. Additionally, the surface tensions of the phases have been rescaled by dividing them by the surface tension of lithium metal to introduce the parameter α_i, defined as $\alpha_i = \frac{\gamma_1}{\gamma_i}$. The electrolyte and lithium phases are assigned a higher interfacial energy ($\alpha_1 = \alpha_0 = 1$), while the interfacial energy of the SEI phases ($\alpha_2 = \alpha_3 = \alpha$) is treated as a variable parameter in the study. These assumptions allow the interfacial parameter α to characterize the thermodynamic stability of the junction between the two SEI domains, meaning that α expresses the interfacial affinity between the SEI phases.

As mentioned by several authors [28,29], multiphase-field can generate spurious phases at the interface. To address this issue and prevent two phases from overlapping, a constraint $\mathcal{G}$[29] is added to the total free energy $\mathcal{F}_{tot}$:

$$\mathcal{G} = \int_{\Omega} \left(1 - \sum_{i=0}^{N-1} \xi_i\right) dV \tag{3}$$

and the matched Lagrange multiplier

$$\beta_i = \frac{-\xi_i^2}{\sum_{j=0}^{N-1} \xi_j^2} \sum_{i=0}^{N-1} \mu_i \tag{4}$$

with $\mu_i = \frac{1}{k_B T}\frac{\delta \mathcal{F}_i}{\delta \xi_i}$ is the chemical potential linked to the order parameter ξ_i.

With this constraint, the dynamical evolution of the order parameter ξ_i is given by the conservation equation with a source term

$$\frac{\partial \xi_i}{\partial t} = \vec{\nabla} \cdot \left[M_i k_B T \vec{\nabla}\left(\mu_i - \beta_i\right)\right] + S_i \tag{5}$$

where M_i is the mobility associated with ξ_i. We should note that, for convenience, the same constant mobility is assumed for all phases (i.e. $M = M_i \quad \forall i$).

The redox reactions are governed by the source term S_i at the interface of each phase. In the first part of this work, as in previous studies [22,23,30–33], electrolyte degradation leading to SEI growth is neglected compared to the plating process (meaning that $S_2 = S_3 = 0$). The influence of SEI growth is subsequently discussed through a dedicated section. Lithium electrodeposition is described by a Butler–Volmer law:

$$S_1 = \tau h'\left(\xi_1\right) \left[\exp\left(\alpha_a \frac{nF}{RT}\eta\right) - \exp\left(-\alpha_c \frac{nF}{RT}\eta\right)\right] \tag{6}$$

where RT is the thermal energy per mole, F is the Faraday constant, n is the number of electrons involved in the redox reaction, α_a and α_c are the charge transfer coefficients associated to the ion oxidation and reduction, τ is the reaction rate constant and η is the overpotential. The function $h'\left(\xi_i\right) = 30\xi_i^2\left(1-\xi_i\right)^2$ is a tracking function used to localize the phase interface associated with ξ_i [23]. To reduce the system's degrees of freedom and avoid non-linear effects, the Butler–Volmer term S_1 is considered at zeroth order. This simplification also minimizes the number of parameters involved in the model, which is particularly relevant since several of these parameters are experimentally inaccessible. Indeed, the experimental characterization of the SEI does not provide sufficient spatial resolution to extract local values of quantities such as the overpotential or the ionic concentration. Yet, such local data would be required in a fully resolved numerical description. Avoiding their explicit use therefore allows us to retain the physical consistency of the model while preventing the introduction of poorly constrained parameters. At the interface between a SEI phase and lithium metal, the lithium-ion concentration and overpotential are assumed to remain constant, which is a reasonable hypothesis for small system deformations [34]. Consequently, the Butler–Volmer term can be simplified to the sum of the constant contribution for each interface of lithium metal domain:

$$S_1 = \tau h'\left(\xi_1\right) \left[h'\left(\xi_0\right) s_0 + h'\left(\xi_2\right) s_2 + h'\left(\xi_3\right) s_3\right] \tag{7}$$

with s_i a parameter proportional to the local current density j_i at the interface between lithium metal and the phase i. Due to the conservative property of the system, the constraint $S_0 = -S_1$ must be imposed.

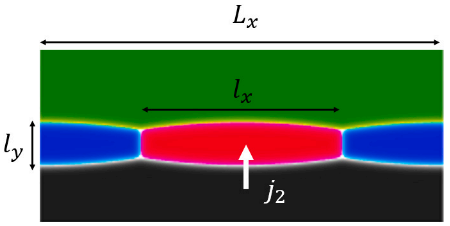

Fig. 1. Initial configuration of a typical simulation box. Lithium domain is denoted in black, the electrolyte in green and the two SEI domains are in blue and red. The ionic insulator or inactive SEI in blue, and the ionic conductive or active SEI in red. The geometrical parameter of the model are also introduced : L_x is the box size and $l_x l_y$ is the initial surface of the conductive SEI, witch is assumed to be the unique domain able to transport Li$^+$ ion, leading to the local density current j_2 at the interface lithium/red SEI.

The characteristic time t_0 and the characteristic scale r_0 of the model are introduced and defined as $\tilde{\vec{r}} = \frac{\vec{r}}{r_0}$ and $\tilde{t} = \frac{t}{t_0}$, where the tildes denote the non-dimensionalized variables. Eq. (5) becomes:

$$\begin{cases} \frac{\partial \xi_i}{\partial \tilde{t}} = \tilde{M} \tilde{\nabla}^2 \left(\tilde{\mu}_i - \tilde{\beta}_i \right) + \tilde{S}_i \\ \tilde{\mu}_i = \frac{\tilde{W}}{\alpha_i} f \left(\xi_i \right) - \frac{\tilde{\kappa}_i}{\alpha_i} \tilde{\nabla}^2 \xi_i \end{cases} \tag{8}$$

where $\tilde{S}_i = t_0 S_i$ and $\tilde{\mu}_i - \tilde{\beta}_i = r_0^3 \left(\mu_i - \beta_i \right)$. The values of the characteristic parameters of each phase are given by

$$\begin{cases} \tilde{\kappa} = \kappa r_0 = 32 \\ \tilde{W} = W r_0^3 = \frac{25}{4} \\ \tilde{M} = M_i k_B T \frac{t_0}{r_0^5} = 1 \end{cases} \tag{9}$$

These parameters are chosen to have a mesh size of $r_0 = 1$ nm. Additionally, it is assumed that the characteristic time t_0 is constant and set to 0.002s. Consequently, the order of magnitude of the diffusion coefficients associated with the order parameters is nm^2.s^{-1}, which is consistent with other phase-field studies on the dendrite scale [22,23,31,35,36].

Furthermore, the system's design parameters are illustrated in Fig. 1. The lithium electrode phase (in black) is completely passivated by a SEI constituted of two domains (blue and red). In this work, one of the SEI domains is assumed to be an ionic insulator (here the blue domain), referred as an inactive domain, hence $s_3 = 0$. The lithium deposition occurs at the interface between the active SEI domain (in red), which is ionically conductive, and the lithium domain. In the event of a SEI crack, leading to a direct contact between the electrolyte (in green) and the electrode, a convergence of the ionic flux at the electrode/electrolyte interface is expected [11,12,26].

To model this phenomenon, the local current density at the electrode/electrolyte interface j_0 is arbitrarily assumed $j_0 = 2j_2$. Nevertheless, the SEI fracture leads to an important energetic modification of the system, complicating the physical interpretation of the order parameters. Post-fracture information is only given for guidance.

The study of Hu et al. [37] enables the identification of the ionic insulator phase as a pure LiF domain, observed on the surface of the SEI layer [19,20,38]. Experimental investigations have identified LiF as an inactive domain that drastically reduces local deposition of the ions [15,16,39,40].

As shown in Fig. 1, the width of the active domain is denoted as l_x and the thickness of the SEI layer is l_y. The simulation box has a size of $L_x \times 400 r_0$.

No-flux conditions are applied at the top and bottom of the simulation box, while periodic boundaries are imposed on the left and right boundaries are periodical. The multiphase-field simulations are performed using a finite element method in Comsol 6.0. The time step is $10 t_0$. The arbitrary fixed parameters are shown in Table 1.

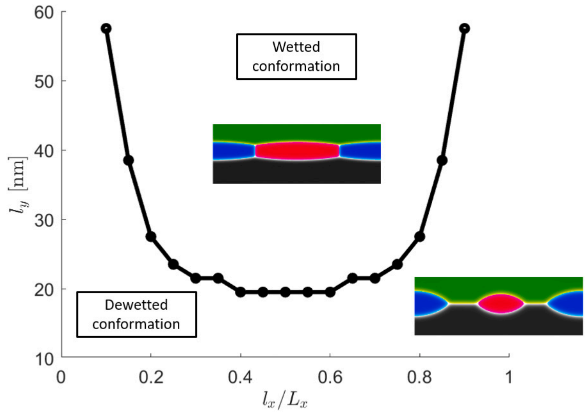

Fig. 2. Wetting diagram for different SEI geometries in a box size $L_x = 200$nm and with a surface tension factor $\alpha = 4$. Due to the mesh size, the spatial resolution is equal to $r_0 = 1$ nm.

Table 1
Multiphase field simulation parameters.

Parameter	Symbol	Dimensionless value
Characteristic size	r_0	1
Characteristic time	t_0	1
Interfacial mobility	M	1
Barrier height	W	$\frac{25}{4}$
Gradient energy coefficient	κ	32
System size	L_x	200
Time step	Δt	10

The studied geometries are determined by thermodynamic considerations. Furthermore, at equilibrium (for $j_2 = 0$), some SEI geometries do not totally passivate lithium metal phase. The SEI layer may dewet and form two domains, leaving regions with a direct contact between lithium metal and the electrolyte. These conformations are not experimentally observed and are not expected due to the degradation of the electrolyte. In Fig. 2, a typical wetting diagram is presented to identify the wetted conformation. For a given surface tension parameter $\alpha = 4$, various thicknesses and active domain widths were studied. A SEI layer with a small active domain $l_x/L_x < 0.2$ is unstable in wetted conformation and needs to be thick enough. A plateau is observed between $0.4 \leq l_x/L_x \leq 0.6$. The diagram is symmetric around $l_x/L_x = 0.5$, which is due to the identical interfacial properties of the SEI domains and the periodic boundary conditions. Under the curve, the interfacial forces are too intense, and the electrolyte is in contact with lithium electrode. Specifically, the size of SEI domains be sufficiently large to avoid phase collapse induced by surface tension. Small SEI domains result in dewetted conformation. Increase the surface tension factor α leads to facilitates the wetted conformation (Fig. S1), the limit is reached for smaller thicknesses.

Subsequently, only wetted geometries are considered.

3. Results

In this study, three system parameters have been studied with the aim to understand the best properties of the SEI to inhibit its failure. These parameters are presented Fig. 1: the thickness of the SEI l_y, the width of the active domain l_x and the surface tension factor α. The interval, where one parameter is probed, is strongly correlated with the value of the two other parameters (Fig. 2). The inhibition of the SEI failure is dependent on the local growth regime of the lithium electrode, proportional to j_2. In this work, the intensity of the local current density has been chosen in the same order of magnitude (0.1 and 10 mA.cm^{-2}) of the applied current density used in computational works [11,22,23,25,26,35]. Although this range is higher than typical

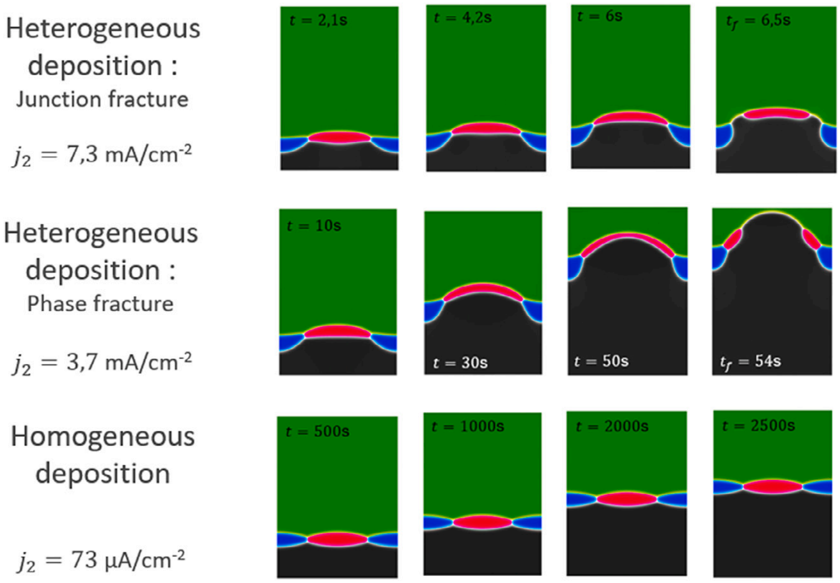

Fig. 3. Different deposition dynamics predicted by the model. The first row shows a junction fracture, under a local current density is $j_2 = 7.3$mA/cm^2. The second row depicts the system's evolution system under a local current density $j_2 = 3.7$mA/cm^2, resulting in a crack in the conductive phase. The third row shows a homogeneous deposition achieved with $j_2 = 73$ µA/cm^2. All examples corresponds to the same system design, with dimensions $l_x = 100$ nm, $l_y = 20$ nm and $\alpha = 4$.

experimental values, it provides a reasonable compromise between realistically perturbing the system and managing computational cost. This choice of current density is particularly relevant for SEI evolution, as it directly influences local ionic fluxes, stress accumulation, and the onset of SEI cracking, all of which play a critical role in dendrite nucleation.

3.1. Deposition regime

Fig. 3 illustrates the evolution of a model interface between lithium metal and an electrolyte, for different local current densities j_2. As a function of the perturbation intensity, three responses have been identified.

In the first row (Fig. 3A, B, C and D), a local current density j_2 of 7.3 mA.cm^{-2} (corresponding to a local lithium electrode growth of 10 nm.s^{-1}) has been used during the simulation. That growth rate is the upper bound in computational approach. Fig. 3A displays the onset of deposition, where lithium grows beneath the active SEI (red domain), whereas Fig. 3B, obtained at a later time, shows the subsequent deformation of the inactive domain. The relaxation of freshly deposited lithium exerts a lateral force on the inactive domain, stretching the active SEI. The relaxation of phases can be tuned by the characteristic time t_0. As deformation increases, the SEI adopts a thermodynamically unfavorable configuration (Fig. 3C), leading to direct contact between the lithium metal and the electrolyte (Fig. 3D). This state is hereafter referred to as SEI failure. In the presented case, the failure of the SEI is located at the junction between both SEI domains. In the absence of lateral favorable interfaces, the SEI domains adopt a droplet shape to minimize interfacial energy. At the fracture site, lithium deposition is significantly enhanced, initiating dendrite nucleation. However, due to model assumptions, this approach is not suited to investigate dendrite geometries, unlike previous models [22,23,25,26,41].

Another deposition regime is shown in the second row (Fig. 3E, F, G and H). This simulation was performed using a local current density $j_2 = 3.7$mA.cm^{-2} (growth of 5 nm.s^{-1}). This simulation exhibits the same steps as those shown in the first row : lithium growth under active SEI (Fig. 3E), deformation of the SEI layer (Fig. 3F), unfavorable conformation (Fig. 3G) and SEI failure (Fig. 3H). the SEI layer undergoes greater deformation, leading to a thinning of the active domain. The bottom and top interfaces overlap, leading to the dewetting of the active domain, which is identified as phase failure.

The third row (Fig. 3I, J, K and L) shows the evolution of the system with a local current density $j_2 = 73$ µA.cm^{-2} (growth of 0.1 nm.s^{-1}). The system stays in a near-equilibrium stationary state, without any significant deformation of the SEI layer, and exhibits homogeneous deposition. In this case, the relaxation of the phases — particularly of freshly reduced lithium — is faster than the applied perturbation j_2.

3.2. Stability of the passivation layer under electrodeposition

The failure of the SEI marks a critical event during which irreversible mechanisms are triggered. The failure time t_f is used as a key observable to assess the SEI's stability under a given deposition rate. To accurately determine t_f, a topological approach is employed to monitor the variation of the interface size of phases. Upon SEI failure, SEI domains significantly reduce their interfacial area in order to adopt a more stable configuration. The maximum value of this interfacial size corresponds to the time step immediately preceding the fracture.

Fig. 4 illustrates the typical evolution of the interfacial length of the active SEI along the simulation presented Fig. 3A, B, C and D. As previously observed qualitatively, heterogeneous lithium electrodeposition leads to a deformation of the active domain. The length of the active domain interface is used as a quantitative observable. The electrode growth deforms the active domain and increases its interface until to reach an unstable configuration, where keeping such a long interface is unfavorable. At $t = t_f = 6.5$s SEI layer fails and the SEI domains are changing their configurations to move toward droplets, with shorter interfaces that are therefore more stable.

Fig. 5 presents the influence of each parameter on the initial geometry. Due to the droplet shape caused by surface tension dynamics, the SEI domain is thicker at the center than at its edges. This asymmetry becomes more pronounced when the SEI ratio l_x/L_x deviates significantly from 0.5 (Fig. 5A, B and C). A larger SEI thickness l_y mitigates the asymmetry (Fig. 5D, E and F). Increasing the surface tension factor α helps suppress the droplet morphology, promoting a more square-shaped SEI domain (Fig. 5G, H and I). Indeed, larger is α smaller is the energetic cost of the SEI–SEI interface, making it more favorable to expand this interface rather than the SEI–lithium or SEI–electrolyte interfaces.

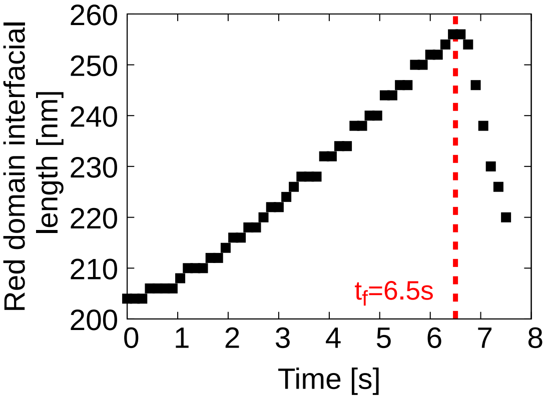

Fig. 4. Evolution of the interface length of the red SEI for the simulation corresponding to the snapshot depicted in the first row of Fig. 3. The parameters are $j_2 = 7.3\text{mA/cm}^2$, $l_x = 100$ nm, $l_y = 20$ nm and $\alpha = 4$.

3.2.1. *Local current density* j_2

As depicted in Fig. 3, the local current density j_2 strongly influences the deposition dynamics, highlighting the competition between the perturbation and the relaxation of the system. Higher currents promote localized stress and SEI deformation, which can lead to cracks and dendrite nucleation, while lower currents favor more uniform deposition and allow the SEI to relax, maintaining a stable interface. The effect of the local current j_2 on the fracture time t_f is illustrated in Fig. 6(a): as expected, higher local current leads to faster fracture. A power-law scaling with an exponent of −2 is observed, consistent with the diffusive relaxation described by the Cahn-Hilliard equation. Between $j_2 = 3\text{mA/cm}^2$ and $j_2 = 6\text{mA/cm}^2$ phase failures are observed (Fig. 3E, F, G and H), in contrast to junction fractures in other simulations of the same system (Fig. 3A, B, C and D).

Regardless of the values of the parameters (l_x, l_y and α), similar scaling laws are observed, regardless of the fracture location (Fig. S3). However, the perturbation range leading to phase failure depends on the SEI geometry; expand it to briefly explain why SEI geometry affects the perturbation range.

3.2.2. *Surface tension factor* α

The surface tension factor α plays a major role in the system geometry (Fig. 5) ; a large α values indicate that the energy of the interface between the two SEI domains is low relative to the SEI–lithium and SEI–electrolyte interfaces. As shown in Fig. 5, reducing the interfacial energy of the SEI interface leads to increase the length of the interface between the two SEI domains.

Fig. 6(b) illustrates the influence of α on the fracture time t_f. In SEI configurations with low α (for $\alpha \leq 8$ for the system shown in Fig. 6(b)), the fracture time t_f increases with α. A characteristic equilibrium geometry of these SEI has been presented Fig. 5G. Indeed, increasing α enhances the stability of the interface between the two SEI domains, allowing the SEI to withstand greater deformation before cracking at the junction.

However, beyond a certain threshold of interfacial parameter α (for $8 < \alpha < 20$ in Fig. 6(b)), the interface between the two SEI domains becomes more important (Fig. 5H) and rigid, causing the system to lose flexibility, particularly at the SEI–SEI interface. To sustain heterogeneous local lithium growth, the active SEI deforms, but the interface stability prevents any further evolution of the junction between the two SEI domains. The deformation of the active domain leads it to become thinner and finally fails. Phase failures occur. For large α values (for $\alpha \geq 20$ in Fig. 6(b)), the passivation layer becomes overly stable (Fig. 5I), and deformation under lithium growth becomes energetically unfavorable. Therefore, the most favorable conformation destabilizes the phases, pushing the system out of equilibrium and causing the electrode to overlap the SEI during ion deposition, which drastically reduces the fracture time t_f. Neither lithium phase nor the conductive SEI remains a pure phase.

Although no mechanical contribution are implemented in the model, this result is qualitatively consistent with experimental observation [18] showing that an excessively rigid SEI is detrimental to fracture inhibition. Finally, we identify the parameter α as the thermodynamic rigidity of the SEI. It is noteworthy that the threshold value depends on the amplitude of the perturbation j_2.

3.2.3. *The width of the conductive SEI* l_x

Due to the potentiostatic approach, a wider active SEI domain results in a larger amount of lithium being deposited at each instant (Fig. 5A, B and C). Although the effective interface of a SEI domain evolves during plating, a notable behavior of the fracture time t_f with respect to the active domain width l_x is observed in Fig. 7(a). When the SEI is predominantly composed of an inactive domain (for $l_x < \frac{L_x}{2}$), the fracture time t_f increases linearly with l_x. Conversely, when the conductive SEI is the main component, t_f reaches a plateau. The transition in fracture type corresponds to the inflection point in the curve, with domain fractures occurring for $l_x > \frac{L_x}{2}$.

A larger active domain (for $l_x > \frac{L_x}{2}$) can accommodate greater deformation and is more effective at delaying fracture. Such a response is reminiscent of a clamped–clamped beam bending under a uniformly distributed load. Greater deformation of the active SEI domain also facilitates phase fractures (Fig. 3). Similarly, a wider conductive region enables more lithium to be deposited (due to the potentiostatic approach), this result is not visible when considering the fracture time alone. In contrast, a SEI layer predominantly composed of an inactive domain (for $l_x < \frac{L_x}{2}$) is limited to smaller deformation — leading to junction fracture — and a small amount of deposited lithium (even at the same deposition rate) before the SEI failure.

To delay SEI fracture, it is preferable to have inactive domains of small size within the SEI. These results are qualitatively coherent with experimental observations [15,16,42].

Although the simulations are formulated in terms of the local current density j_2, the physical interpretation of the results must be understood in relation to the effective amount of lithium accommodated by the deforming active SEI domain. Wider active domains are able to undergo larger deformations, which increases the effective lithium deposition surface and allows a larger amount of lithium to be incorporated before localization occurs. As a result, for a given value of j_2, wider active regions can sustain more homogeneous ionic flux distributions, whereas narrow active domains rapidly concentrate deposition at their boundaries. In this latter case, deformation is strongly constrained by neighboring inactive regions, and phase rupture preferentially initiates at SEI–SEI interfaces rather than through progressive deformation of the active domain itself.

3.2.4. *The thickness of the SEI* l_y

As shown in Fig. 5, increasing the SEI thickness enhances the interfacial junction between the two SEI domains, thereby improving its stability. Fig. 7(b) illustrates the fracture time t_f as a function of SEI thickness l_y. For thin layers, t_f increases sharply with l_y, then a plateau appears. Interestingly, for SEI thicknesses above 35 nm, t_f begins to decrease. This turning point corresponds to a bifurcation in the failure mode. As l_y increases, the thermodynamic stiffness of the SEI is enhanced. The SEI thickness plays a role analogous to the surface tension factor α. We hypothesize a relationship between these two parameters, possibly linked to an underlying variable describing the thermodynamic rigidity of the SEI. This will be explored in future work. The final drop in the curve reflects a mathematical limitation of the model. For lithium growth to occur, the electrolyte must be displaced from the interface between the active SEI and the electrode. This displaced electrolyte is replenished via diffusion through the SEI. As SEI thickness increases, this process becomes slower. If the diffusion time

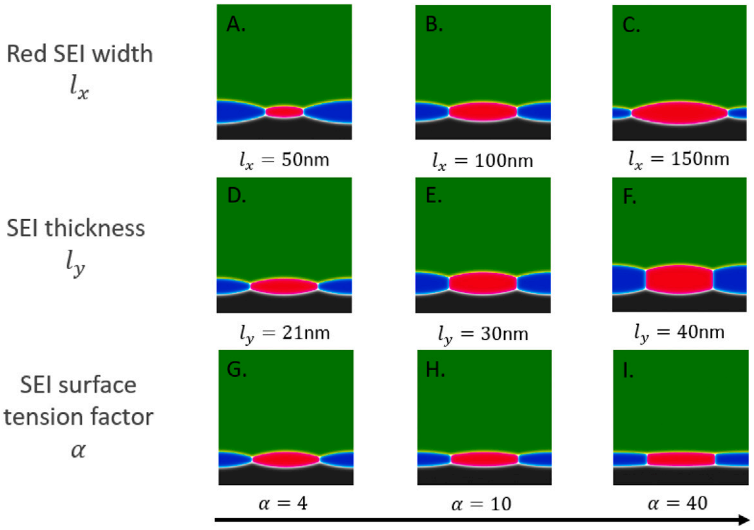

Fig. 5. On the first row, initial geometries for various active SEI width l_x are presented for SEI thickness $l_y = 25$ nm and the surface tension factor $\alpha = 4$. The second row illustrates the effect of varying SEI thickness l_y on the initial conformation with $l_x = 100$ nm and $\alpha = 4$. The final row illustrates the effect of varying surface tension factor α on the equilibrium geometry, with $l_x = 100$ nm and $l_y = 20$ nm.

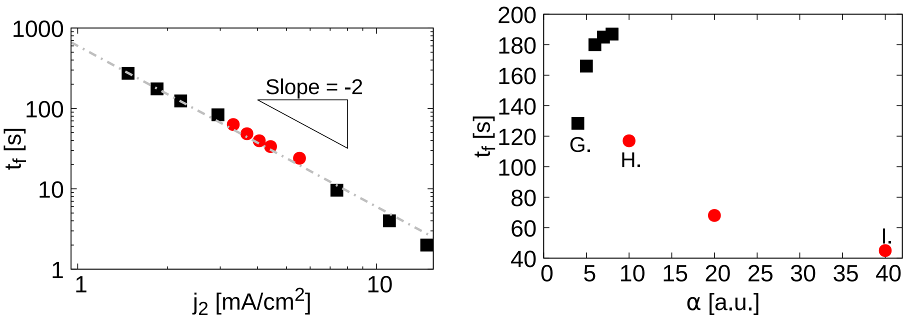

(a) SEI failure time t_f as a function of the local current density j_2. The dotted line represents the scaling law obtained by fitting. These results were obtained with $l_y = 20$ nm, $\alpha = 4$ and $j_2 = 7.3$mA/cm².

(b) SEI failure time for different SEI surface tension factor α. These results were obtained with $l_x = 100$ nm, $l_y = 21$ nm and $\alpha = 4$.

Fig. 6. Different markers are used to indicate the fracture type: black squares denote junction fractures while red circles represent phase fractures. The letters refer to configurations illustrated in Fig. 1.

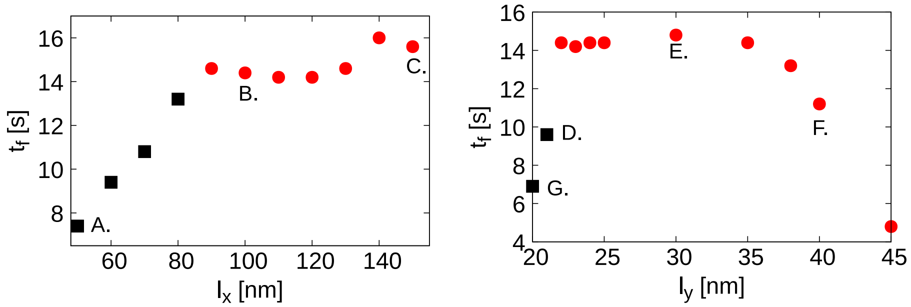

(a) SEI failure time t_f for different width of the conductive SEI l_x. These results were obtained with $l_y = 20$ nm, $\alpha = 4$ and $j_2 = 7.3$mA/cm².

(b) SEI failure time t_f for different SEI thickness l_y. These results were obtained with $l_x = 100$ nm, $\alpha = 4$ and $j_2 = 7.3$mA/cm².

Fig. 7. SEI failure time t_f for different geometrical parameters. Different markers are used to indicate the fracture type : black squares denote junction fractures while red circles represent phase fractures. The letters refer to configurations illustrated in Fig. 1.

exceeds the perturbation timescale, electrolyte displacement becomes incomplete, pushing the SEI phases out of equilibrium and accelerating fracture. It is worth noting that the critical thickness of 35 nm depends on the deposition rate; at lower current densities, this threshold is higher.

As shown in Fig. 5, increasing the SEI thickness enhances the interfacial junction between the two SEI domains, thereby improving its stability. Fig. 7(b) illustrates the fracture time t_f as a function of SEI thickness l_y. For thin layer, t_f increases sharply with l_y, then a plateau appears. Interestingly, for SEI thicknesses above 35 nm, t_f begins to decrease. This turning point corresponds to a bifurcation in the failure mode.

As l_y increases, the thermodynamic stiffness of the SEI is enhanced. The SEI thickness plays a role analogous to the surface tension factor α. We hypothesize a relationship between these two parameters, possibly linked to an underlying variable describing the thermodynamic rigidity of the SEI. This will be explored in future work.

The final drop in the curve can be rationalized by comparing characteristic timescales. For lithium growth to occur, the electrolyte must be displaced from the interface between the active SEI and the electrode. This displaced electrolyte is replenished via diffusion through the SEI, with a characteristic diffusion time scaling as $t_{\mathrm{diff}} \propto l_y^2 t_0 / r_0^2$. As SEI thickness increases, this process becomes progressively slower. When this diffusion time becomes comparable to or larger than the characteristic timescale associated with lithium-deposition-induced perturbations, the electrolyte cannot fully relax local concentration gradients, pushing the SEI phases out of equilibrium and accelerating fracture.

Accordingly, the critical thickness of approximately 35 nm identified here corresponds to a crossover regime rather than to an intrinsic material constant. It is worth noting that this threshold depends on the deposition rate; at lower current densities, this critical thickness is shifted to higher values, as illustrated in Tab. S1.

When the active SEI domain is sufficiently thick or wide, its deformation modifies the local geometry of the electrode–electrolyte interface and leads to a redistribution of ionic fluxes. In addition to flux components normal to the initial interface, lateral ionic fluxes emerge along the deformed SEI surface. These lateral fluxes promote lithium deposition parallel to the interface, which in turn further stretches the active domain by displacing adjacent inactive regions. This mechanism establishes a positive feedback loop in which deformation enhances lateral deposition, leading to additional deformation. The process continues until the active domain reaches its mechanical or geometrical limit and eventually fractures. This feedback mechanism provides a physical explanation for the dependence of the phase-rupture regime on SEI geometry and for the spatial extent of the perturbed region observed in the simulations.

3.3. *Preliminary study of electrolyte degradation reactions*

In a real system, the electrolyte progressively degrades over successive charge–discharge cycles [8,13], leading to an evolution of the solid electrolyte interphase (SEI) that alters its thickness, composition, and mechanical properties. Such degradation processes may therefore significantly influence the fracture dynamics observed in the proposed model. For a stable SEI, which is typically relatively thick (Fig. 2), it is not relevant to account for continuous electrolyte degradation over the time scales considered here (on the order of tens of seconds). Indeed, in the absence of interfacial overpotential and faradaic current, once the SEI layer has formed, its evolution occurs over much longer time scales. Nevertheless, situations in which the SEI becomes insufficiently thick — and thus unstable — must still be addressed. The most critical case corresponds to fracture regions, where freshly exposed lithium is brought into direct contact with the electrolyte, thereby promoting rapid degradation reactions. To model this mechanism, the same formalism as that used for lithium-ion electrodeposition reactions (Eq. (7)) can be employed.

$$\begin{cases} S_2 = \tau_{\mathrm{SEI}} s_{\mathrm{SEI},2} \left[h'\left(\xi_0\right) \times h'\left(\xi_1\right) \right] \\ S_3 = \tau_{\mathrm{SEI}} s_{\mathrm{SEI},3} \left[h'\left(\xi_0\right) \times h'\left(\xi_1\right) \right] \end{cases} \tag{10}$$

where τ_{SEI} is the reaction time constant associated with the formation of SEI domains, and $s_{\mathrm{SEI},2}$ and $s_{\mathrm{SEI},3}$ denote the reaction strengths of the active and inactive SEI phases, respectively. The product $h'\left(\xi_0\right) \times h'\left(\xi_1\right)$ is used to localize the interface between metallic lithium and the electrolyte. Within this framework, the conservative formulation imposes $S_0 = -\left(S_1 + S_2 + S_3\right)$. In practice, when the interfaces of the electrolyte and metallic lithium phases overlap — i.e., when the local SEI thickness is smaller than $2\lambda \simeq 5$ nm, — the growth of either an SEI phase or the electrode phase necessarily implies the consumption of the electrolyte phase. Direct local measurements of the products $\tau_{\mathrm{SEI}} s_{\mathrm{SEI},2}$ and $\tau_{\mathrm{SEI}} s_{\mathrm{SEI},3}$ remain an experimental challenge. To assess the sensitivity of the model to these parameters, we therefore introduce the observables k_2 and k_3 defined as:

$$\begin{cases} k_2 = \frac{\tau_{\mathrm{SEI}} s_{\mathrm{SEI},2}}{\tau s_2} \propto \frac{\tau_{\mathrm{SEI}} s_{\mathrm{SEI},2}}{j_2} \\ k_3 = \frac{\tau_{\mathrm{SEI}} s_{\mathrm{SEI},3}}{\tau s_2} \propto \frac{\tau_{\mathrm{SEI}} s_{\mathrm{SEI},3}}{j_2} \end{cases} \tag{11}$$

Accordingly, when k_2 and k_3 are smaller than unity, lithium-ion electrodeposition reactions are favored, whereas degradation reactions dominate when these parameters exceed unity. For the present sensitivity study, we focus on a fixed SEI geometry ($l_x = 100$ nm, $l_y = 20$ nm and $\alpha = 4$) subjected to a perturbation current density of $j_2 = 7.3\mathrm{mA.cm}^{-2}$. Fig. 8 shows the system after a deposition phase for various values of the observables k_2 et k_3. Figs. 8(a) and 8(b) illustrate cases in which degradation reactions are weaker than electrodeposition, after nine seconds of plating. When the growth of the active SEI domain is faster (Fig. 8(b)), in addition to the growth of the conductive domain, the nucleation of a new active SEI domain at the electrode surface can be observed. Conversely, when the growth of the inactive SEI domain is faster (Fig. 8(a)), the insulating SEI grows and forms a column within the electrode. At the lithium metal–electrolyte interface, the growth of the insulating SEI is sufficiently rapid to induce the nucleation of inactive SEI domains.

When both SEI phases exhibit growth rates of the same order of magnitude and sufficiently high (Fig. 8(c)), the inactive domain becomes trapped within the electrode (the temporal evolution of the interface is provided in Fig. S4), while the active domain covers the electrode, preventing future dendrite nucleation. The interface morphology after 19 s for $k_2 = 0.01$ and $k_3 = 1$ is shown in Fig. 8(d). A significant increase in the volume of the inactive domain can be observed, taking the form of a column. The SEI remains stable and does not fracture, thereby limiting dendrite nucleation; however, the deposition remains non-uniform. More generally, we observe that when the SEI growth dynamics are of the same order of magnitude as, or faster than, the deposition dynamics (i.e. $k_2 \geq 1$ or $k_3 \geq 1$), the SEI remains stable. Table 2 summarizes the fracture times as a function of k_2 and k_3 for the considered system. When reaction rates are negligible ($k_2 = 0.01$ et $k_3 = 0.01$), no significant change in the fracture time t_f is observed, and the results remain within the measurement uncertainty compared to the case without degradation reactions. When the reaction intensities are smaller than the deposition rate ($k_2 = 0.1$ et $k_3 = 0.1$) SEI formation delays fracture by a few tenths of a second. For the case $k_2 = 0.1$ et $k_3 = 1$, we observe the formation of a phase fracture within the active domain. The degradation reactions of the inactive domain are nevertheless sufficiently intense to induce the nucleation of an inactive domain at the fracture site and stabilize the interface. This case is discussed in detail in the Supporting Information.

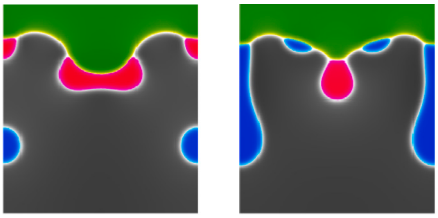

(a) k_2 = 0.01 and k_3 = 0.1 after 9 s

(b) k_2 = 0.1 and k_3 = 0.01 after 9 seconds

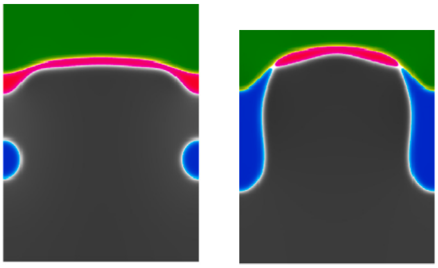

(c) k_2 = 1 and k_3 = 1 after 17 s

(d) k_2 = 0.01 and k_3 = 1 after 19 s

Fig. 8. Representative system conformations observed at different deposition times for selected combinations of k_2 and k_3.

Table 2
Fracture time t_f for an SEI with the following properties: l_x = 100 nm, l_y = 20 nm, and α = 4, for different SEI domain formation rates. The local current density is j_2 = 7.3 mA cm^{-2}. The case marked with an asterisk is distinguished by a fracture of the SEI followed by repassivation of the electrode.

		k_2			
		0	0.01	0.1	1
k_3	0	6.5s	6.8s	7.0s	Stable
	0.01	6.8s	6.8s	7.0s	Stable
	0.1	7.0s	7.0s	7.1s	18.2s*
	1	Stable	Stable	Stable	Stable

4. Conclusion

In summary, a novel multiphase-field model has been introduced to investigate the dendrite nucleation during lithium plating. This approach allows a more sophisticated modeling of the SEI that the previous computational works [12,22–26]: with a dynamical and heterogeneous SEI. To improve this, the study scale focused on the SEI failure which leads to dendrite nucleation and dendrite formation. While some contributions at the lithium/electrolyte interface are yet to be implemented (such as electrolyte reduction and mechanical effects), two distinct deposition regimes have been identified:

- At low current densities, perturbations remain sufficiently small to allow relaxation of the freshly deposited lithium, leading to homogeneous deposition.
- At high current regimes, perturbations evolve faster than relaxation, leading to SEI fracture, which can occur either within the active SEI phase (phase fracture) or at the boundaries between SEI domains (junction fracture).

These regimes are in good agreement with computational studies [12,22–26,41]. Phase fractures and junction fractures are inherent to the dynamic multidomain SEI modeling and, to the best of our knowledge, are identified here for the first time.

To study the stability of the SEI — in terms of delaying fracture due to heterogeneous lithium ion deposition — the fracture time t_f was defined as a key observable. Based on a SEI model configuration, we conducted a parametric study of the geometric and interfacial properties of the system. Since the SEI structure is largely dependent on the electrolyte [15,16,39,43], the design of the SEI model is therefore conditioned by the studied system. A sensitivity analysis was conducted to assess the influence of electrolyte degradation reactions on SEI stability. To effectively delay SEI fracture — or even inhibit it — at least one SEI domain must exhibit a growth rate of the same order of magnitude as that of lithium deposition. It is worth noting, however, that fracture inhibition alone is not a sufficient criterion to ensure homogeneous electrode growth.

The SEI's ability to deform is a crucial factor for its stability during electrodeposition. In fact, the deformation allows the SEI to accommodate and support the growth of the lithium metal electrode. However, the SEI must retain sufficient rigidity to promote homogeneous lithium metal electrode growth. This balance between rigidity and deformability also depends on the ion deposition rate. From an applied point of view, this suggests that SEI layers composed of many small inactive domains (such as LiF) are more effective at preventing SEI cracking and dendrite formation than those with fewer large inactive regions. This conclusion is consistent with experimental observations [15,16,42].

The dynamic system is driven by the competition between minimizing the interfacial areas of each phase and electrochemical reactions. These two processes have been modeled under significant assumptions, primarily because of the lack of numerical and experimental data at relevant scales. To address these limitations, it will be necessary to implement ionic concentration and electrostatic potential fields to remove the assumption of constant overpotential along the interfaces. Additionally, due to strong mechanical heterogeneities, incorporating elastic contributions — which appear sufficient given the observed deformations [38] — would allow the investigation of interfaces with preferential deformation regions that counter droplet-like conformations.

Finally, experimental validation will require coupling with in-situ characterization methods: AFM or SEM to monitor surface topology evolution and associated deformations, and AES or XPS to identify SEI failure. However, the characteristic length scales involved in SEI junction and phase fracture are on the order of a few tens of nanometers, which currently challenges the spatial resolution and depth sensitivity of most operando techniques applicable to reactive lithium interfaces. Interestingly, although lithium migration induced by the electron beam in AES currently limits quantitative chemical analysis, this effect could potentially be exploited as a contrast mechanism to identify regions with enhanced lithium transport, such as SEI junctions or active domains. Future advances in high-resolution surface-sensitive characterization, possibly combining local chemical mapping with AFM-based electrical probing, will be essential to directly assess these failure modes.

The model has been designed with modularity in mind, facilitating the future implementation of additional features such as mechanical effects, multiple SEI domains, and the crystallographic anisotropy of the lithium metal. These enhancements will be addressed in future work.

CRediT authorship contribution statement

Thibault Delpech: Writing – original draft, Visualization, Validation, Software, Methodology, Conceptualization. **Benoit Chavillon:** Writing – review & editing. **Sébastien Martinet:** Writing – review & editing. **Anass Benayad:** Writing – review & editing. **Hervé Manzanarez:** Writing – review & editing, Validation, Project administration, Methodology, Conceptualization.

Declaration of competing interest

The authors declare that they have no known competing financial interests or personal relationships that could have appeared to influence the work reported in this paper.

Appendix A. Supplementary data

Supplementary material related to this article can be found online at https://doi.org/10.1016/j.jpowsour.2026.239657.

Data availability

No data was used for the research described in the article.

References

[1] D. Lin, Y. Liu, Y. Cui, Reviving the lithium metal anode for high-energy batteries, Nature Nanotechnology 12 (3) (2017) 194–206, http://dx.doi.org/10.1038/nnano.2017.16, Publisher: Nature Publishing Group. URL https://www.nature.com/articles/nnano.2017.16.

[2] A. Kushima, K.P. So, C. Su, P. Bai, N. Kuriyama, T. Maebashi, Y. Fujiwara, M.Z. Bazant, J. Li, Liquid cell transmission electron microscopy observation of lithium metal growth and dissolution: Root growth, dead lithium and lithium flotsams, Nano Energy 32 (2017) 271–279, http://dx.doi.org/10.1016/j.nanoen.2016.12.001, URL https://linkinghub.elsevier.com/retrieve/pii/S2211285516305651.

[3] J.K. Stark, Y. Ding, P.A. Kohl, Nucleation of electrodeposited lithium metal: Dendritic growth and the effect of co-deposited sodium, J. Electrochem. Soc. 160 (9) (2013) D337, http://dx.doi.org/10.1149/2.028309jes, Publisher: IOP Publishing. URL https://iopscience.iop.org/article/10.1149/2.028309jes/meta.

[4] H.J. Sand, III. on the concentration at the electrodes in a solution, with special reference to the liberation of hydrogen by electrolysis of a mixture of copper sulphate and sulphuric acid, Lond. Edinb. Dublin Philos. Mag. J. Sci. 1 (1) (1901) 45–79, http://dx.doi.org/10.1080/14786440109462590, Publisher: Taylor & Francis _eprint.

[5] M. Rosso, T. Gobron, C. Brissot, J.N. Chazalviel, S. Lascaud, Onset of dendritic growth in lithium/polymer cells, J. Power Sources 97–98 (2001) 804–806, http://dx.doi.org/10.1016/S0378-7753(01)00734-0, URL https://www.sciencedirect.com/science/article/pii/S0378775301007340.

[6] P.G. Kitz, M.J. Lacey, P. Novák, E.J. Berg, Operando investigation of the solid electrolyte interphase mechanical and transport properties formed from vinylene carbonate and fluoroethylene carbonate, J. Power Sources 477 (2020) 228567, http://dx.doi.org/10.1016/j.jpowsour.2020.228567, URL https://www.sciencedirect.com/science/article/pii/S0378775320308715.

[7] A. Benayad, J.E. Morales-Ugarte, C.C. Santini, R. Bouchet, Operando XPS: A novel approach for probing the lithium/Electrolyte interphase dynamic evolution, J. Phys. Chem. A 125 (4) (2021) 1069–1081, http://dx.doi.org/10.1021/acs.jpca.0c09047, Publisher: American Chemical Society.

[8] J.E. Morales-Ugarte, A. Benayad, C.C. Santini, R. Bouchet, Electrochemical impedance spectroscopy and X-ray photoelectron spectroscopy study of lithium metal surface aging in imidazolium-based ionic liquid electrolytes performed at open-circuit voltage, ACS Appl. Mater. Interfaces 11 (24) (2019) 21955–21964, http://dx.doi.org/10.1021/acsami.9b00753.

[9] P.-C. Hsu, Y.-C. Lin, W.-H. Wu, C.-W. Pao, C.-H. Chen, Atomistic investigation of solid electrolyte interphase: nanostructure, chemical composition and mechanical properties, J. Electrochem. Soc. 169 (12) (2022) 120520, http://dx.doi.org/10.1149/1945-7111/acaad2, Publisher: IOP Publishing.

[10] Z. Liu, P. Lu, Q. Zhang, X. Xiao, Y. Qi, L.-Q. Chen, A bottom-up formation mechanism of solid electrolyte interphase revealed by isotope-assisted time-of-flight secondary ion mass spectrometry, J. Phys. Chem. Lett. 9 (18) (2018) 5508–5514, http://dx.doi.org/10.1021/acs.jpclett.8b02350, Publisher: American Chemical Society.

[11] X. Shen, R. Zhang, X. Chen, X.-B. Cheng, X. Li, Q. Zhang, The failure of solid electrolyte interphase on li metal anode: Structural uniformity or mechanical strength? Adv. Energy Mater. 10 (10) (2020) 1903645, http://dx.doi.org/10.1002/aenm.201903645, URL https://onlinelibrary.wiley.com/doi/abs/10.1002/aenm.201903645.

[12] F. Hao, A. Verma, P.P. Mukherjee, Mechanistic insight into dendrite–SEI interactions for lithium metal electrodes, J. Mater. Chem. A 6 (40) (2018) 19664–19671, http://dx.doi.org/10.1039/C8TA07997H, Publisher: The Royal Society of Chemistry. URL https://pubs.rsc.org/en/content/articlelanding/2018/ta/c8ta07997h.

[13] R. Bouchet, S. Lascaud, M. Rosso, An EIS study of the anode Li/PEO-LiTFSI of a Li polymer battery, J. Electrochem. Soc. 150 (10) (2003) A1385, http://dx.doi.org/10.1149/1.1609997, Publisher: IOP Publishing. URL https://iopscience.iop.org/article/10.1149/1.1609997/meta.

[14] C. Brissot, M. Rosso, J.N. Chazalviel, P. Baudry, S. Lascaud, In situ study of dendritic growth inlithium/PEO-salt/lithium cells, Electrochim. Acta 43 (10) (1998) 1569–1574, http://dx.doi.org/10.1016/S0013-4686(97)10055-X, URL https://www.sciencedirect.com/science/article/pii/S001346869710055X.

[15] Z.L. Brown, S. Jurng, C.C. Nguyen, B.L. Lucht, Effect of fluoroethylene carbonate electrolytes on the nanostructure of the solid electrolyte interphase and performance of lithium metal anodes, ACS Appl. Energy Mater. 1 (7) (2018) 3057–3062, http://dx.doi.org/10.1021/acsaem.8b00705, Publisher: American Chemical Society.

[16] S. Jurng, Z.L. Brown, J. Kim, B.L. Lucht, Effect of electrolyte on the nanostructure of the solid electrolyte interphase (SEI) and performance of lithium metal anodes, Energy Environ. Sci. 11 (9) (2018) 2600–2608, http://dx.doi.org/10.1039/C8EE00364E, Publisher: The Royal Society of Chemistry. URL https://pubs.rsc.org/en/content/articlelanding/2018/ee/c8ee00364e.

[17] J. Wang, W. Huang, A. Pei, Y. Li, F. Shi, X. Yu, Y. Cui, Improving cyclability of li metal batteries at elevated temperatures and its origin revealed by cryo-electron microscopy, Nat. Energy 4 (8) (2019) 664–670, http://dx.doi.org/10.1038/s41560-019-0413-3, Publisher: Nature Publishing Group. URL https://www.nature.com/articles/s41560-019-0413-3.

[18] W.-W. Wang, Y. Gu, H. Yan, S. Li, J.-W. He, H.-Y. Xu, Q.-H. Wu, J.-W. Yan, B.-W. Mao, Evaluating solid-electrolyte interphases for lithium and lithium-free anodes from nanoindentation features, Chem 6 (10) (2020) 2728–2745, http://dx.doi.org/10.1016/j.chempr.2020.07.014, URL https://www.sciencedirect.com/science/article/pii/S2451929420303648.

[19] D. Aurbach, Review of selected electrode–solution interactions which determine the performance of li and li ion batteries, J. Power Sources 89 (2) (2000) 206–218, http://dx.doi.org/10.1016/S0378-7753(00)00431-6, URL https://linkinghub.elsevier.com/retrieve/pii/S0378775300004316.

[20] E. Peled, D. Golodnitsky, G. Ardel, Advanced model for solid electrolyte interphase electrodes in liquid and polymer electrolytes, J. Electrochem. Soc. 144 (8) (1997) L208–L210, http://dx.doi.org/10.1149/1.1837858, URL https://iopscience.iop.org/article/10.1149/1.1837858.

[21] M.Y. Yang, S.V. Zybin, T. Das, B.V. Merinov, W.A. Goddard, E.K. Mok, H.J. Hah, H.E. Han, Y.C. Choi, S.H. Kim, Characterization of the solid electrolyte interphase at the li metal–ionic liquid interface, Adv. Energy Mater. 13 (3) (2023) 2202949, http://dx.doi.org/10.1002/aenm.202202949, _eprint: https://onlinelibrary.wiley.com/doi/pdf/10.1002/aenm.202202949.

[22] V. Yurkiv, T. Foroozan, A. Ramasubramanian, R. Shahbazian-Yassar, F. Mashayek, Phase-field modeling of solid electrolyte interface (SEI) influence on li dendritic behavior, Electrochim. Acta 265 (2018) 609–619, http://dx.doi.org/10.1016/j.electacta.2018.01.212, URL https://www.sciencedirect.com/science/article/pii/S0013468618302809.

[23] L. Chen, H.W. Zhang, L.Y. Liang, Z. Liu, Y. Qi, P. Lu, J. Chen, L.-Q. Chen, Modulation of dendritic patterns during electrodeposition: A nonlinear phase-field model, J. Power Sources 300 (2015) 376–385, http://dx.doi.org/10.1016/j.jpowsour.2015.09.055, URL https://linkinghub.elsevier.com/retrieve/pii/S0378775315303141.

[24] G. Yoon, S. Moon, G. Ceder, K. Kang, Deposition and stripping behavior of lithium metal in electrochemical system: Continuum mechanics study, Chem. Mater. 30 (19) (2018) 6769–6776, http://dx.doi.org/10.1021/acs.chemmater.8b02623, Publisher: American Chemical Society.

[25] A. Cipolla, C. Barchasz, B. Mathieu, B. Chavillon, S. Martinet, Effect of electrochemical and mechanical properties of SEI on dendritic growth during lithium deposition on lithium metal electrode, J. Power Sources 545 (2022) 231898, http://dx.doi.org/10.1016/j.jpowsour.2022.231898, URL https://www.sciencedirect.com/science/article/pii/S0378775322008837.

[26] G. Liu, W. Lu, A model of concurrent lithium dendrite growth, SEI growth, SEI penetration and regrowth, J. Electrochem. Soc. 164 (9) (2017) A1826, http://dx.doi.org/10.1149/2.0381709jes, Publisher: IOP Publishing. URL https://iopscience.iop.org/article/10.1149/2.0381709jes/meta.

[27] N. Sitapure, H. Lee, F. Ospina-Acevedo, P.B. Balbuena, S. Hwang, J.S.-I. Kwon, A computational approach to characterize formation of a passivation layer in lithium metal anodes, AIChE J. 67 (1) (2021) e17073, http://dx.doi.org/10.1002/aic.17073, _eprint: https://onlinelibrary.wiley.com/doi/pdf/10.1002/aic.17073.

[28] F. Boyer, C. Lapuerta, S. Minjeaud, B. Piar, M. Quintard, Cahn–hilliard/Navier–Stokes model for the simulation of three-phase flows, Transp. Porous Media 82 (3) (2010) 463–483, http://dx.doi.org/10.1007/s11242-009-9408-z, URL http://link.springer.com/10.1007/s11242-009-9408-z.

[29] H.G. Lee, J. Kim, An efficient numerical method for simulating multiphase flows using a diffuse interface model, Phys. A 423 (2015) 33–50, http://dx.doi.org/10.1016/j.physa.2014.12.027, URL https://linkinghub.elsevier.com/retrieve/pii/S0378437114010693.

[30] L. Gao, Z. Guo, Phase-field simulation of li dendrites with multiple parameters influence, Comput. Mater. Sci. 183 (2020) 109919, http://dx.doi.org/10.1016/j.commatsci.2020.109919, URL https://www.sciencedirect.com/science/article/pii/S0927025620304109.

[31] C.-H. Chen, C.-W. Pao, Phase-field study of dendritic morphology in lithium metal batteries, J. Power Sources 484 (2021) 229203, http://dx.doi.org/10.1016/j.jpowsour.2020.229203, URL https://www.sciencedirect.com/science/article/pii/S0378775320314919.

[32] Y. Zhao, R. Wang, E. Martinez-Paneda, A phase field electro-chemo-mechanical formulation for predicting void evolution at the li–electrolyte interface in all-solid-state batteries, J. Mech. Phys. Solids 167 (2022) 104999, http://dx.doi.org/10.1016/j.jmps.2022.104999, Publisher: Pergamon. URL https://www.sciencedirect.com/science/article/pii/S0022509622001879.

[33] R. Zhang, X. Shen, Y.-T. Zhang, X.-L. Zhong, H.-T. Ju, T.-X. Huang, X. Chen, J.-D. Zhang, J.-Q. Huang, Dead lithium formation in lithium metal batteries: A phase field model, J. Energy Chem. 71 (2022) 29–35, http://dx.doi.org/10.1016/j.jechem.2021.12.020, Publisher: Elsevier. URL https://www.sciencedirect.com/science/article/pii/S2095495621006823.

[34] R. Akolkar, Mathematical model of the dendritic growth during lithium electrodeposition, J. Power Sources 232 (2013) 23–28, http://dx.doi.org/10.1016/j.jpowsour.2013.01.014, URL https://www.sciencedirect.com/science/article/pii/S0378775313000323.

[35] W. Mu, X. Liu, Z. Wen, L. Liu, Numerical simulation of the factors affecting the growth of lithium dendrites, J. Energy Storage 26 (2019) 100921, http://dx.doi.org/10.1016/j.est.2019.100921, URL https://www.sciencedirect.com/science/article/pii/S2352152X19304268.

[36] D.R. Ely, A. Jana, R.E. García, Phase field kinetics of lithium electrodeposits, J. Power Sources 272 (2014) 581–594, http://dx.doi.org/10.1016/j.jpowsour.2014.08.062, URL https://www.sciencedirect.com/science/article/pii/S0378775314013172.

[37] T. Hu, J. Tian, F. Dai, X. Wang, R. Wen, S. Xu, Impact of the local environment on li ion transport in inorganic components of solid electrolyte interphases, J. Am. Chem. Soc. 145 (2) (2023) 1327–1333, http://dx.doi.org/10.1021/jacs.2c11521, Publisher: American Chemical Society.

[38] I. Yoon, S. Jurng, D.P. Abraham, B.L. Lucht, P.R. Guduru, Measurement of mechanical and fracture properties of solid electrolyte interphase on lithium metal anodes in lithium ion batteries, Energy Storage Mater. 25 (2020) 296–304, http://dx.doi.org/10.1016/j.ensm.2019.10.009, URL https://www.sciencedirect.com/science/article/pii/S2405829719310050.

[39] A.C. Thenuwara, P.P. Shetty, M.T. McDowell, Distinct nanoscale interphases and morphology of lithium metal electrodes operating at low temperatures, Nano Lett. 19 (12) (2019) 8664–8672, http://dx.doi.org/10.1021/acs.nanolett.9b03330, Publisher: American Chemical Society.

[40] A.C. Thenuwara, P.P. Shetty, N. Kondekar, S.E. Sandoval, K. Cavallaro, R. May, C.-T. Yang, L.E. Marbella, Y. Qi, M.T. McDowell, Efficient low-temperature cycling of lithium metal anodes by tailoring the solid-electrolyte interphase, ACS Energy Lett. 5 (7) (2020) 2411–2420, http://dx.doi.org/10.1021/acsenergylett.0c01209, Publisher: American Chemical Society.

[41] D. Tewari, P.P. Mukherjee, Mechanistic understanding of electrochemical plating and stripping of metal electrodes, J. Mater. Chem. A 7 (9) (2019) 4668–4688, http://dx.doi.org/10.1039/C8TA11326B, Publisher: The Royal Society of Chemistry. URL https://pubs.rsc.org/en/content/articlelanding/2019/ta/c8ta11326b.

[42] R. Guo, K.-H. Kim, B.M. Gallant, Impact of lif particle morphology on overpotential and structure of li metal deposition, J. Electrochem. Soc. 169 (10) (2022) 100523, http://dx.doi.org/10.1149/1945-7111/ac98e3, Publisher: IOP Publishing.

[43] J.Y. Kim, D.O. Shin, T. Chang, K.M. Kim, J. Jeong, J. Park, Y.M. Lee, K.Y. Cho, C. Phatak, S. Hong, Y.-G. Lee, Effect of the dielectric constant of a liquid electrolyte on lithium metal anodes, Electrochim. Acta 300 (2019) 299–305, http://dx.doi.org/10.1016/j.electacta.2019.01.113, URL https://www.sciencedirect.com/science/article/pii/S0013468619301306.